East European Journal of Physics. 3. 239–250 (2026)
DOI: 10.26565/2312-4334-2026-3-19 ISSN 2312-4334

EMERGENCE OF NEGATIVE DISPERSION OF ELECTROMAGNETIC WAVES IN A SOLID-STATE STRUCTURE CONTAINING A PLASMA-LIKE MEDIUM AND PLASMONIC METASURFACES

Yu.O. Averkov*, O.Yu. Averkov, N.N. Beletskii
O. Ya. Usikov Institute for Radiophysics and Electronics of the National Academy of Sciences of Ukraine, 12, Acad. Proskura Str., Kharkiv, 61085, Ukraine
Corresponding Author e-mail: yuriyaverkov@gmail.com
Received May 12, 2026; revised August 21, 2026; accepted August 26, 2026

This study provides a detailed theoretical and numerical account of the dispersion properties of p-polarized electromagnetic waves in a complex multilayered solid-state structure. The system under investigation is a six-layer stack featuring two isotropic plasmonic metasurfaces, separated by dielectric spacers and supported by a semi-infinite plasma-like substrate—either a heavily doped semiconductor or a metal. By combining the transfer-matrix formalism with Maxwell's equations and rigorous boundary conditions, we derive exact dispersion relations for both surface and bulk-surface eigenmodes. Our numerical results point to a cascaded hybridization process between the fundamental metasurface resonances and the surface plasmon-polariton (SPP) modes inherent to the substrate. A particularly significant finding is that adjusting the effective oscillator strengths of the metasurfaces triggers a pronounced dispersion asymmetry. This occurs when one metasurface exhibits a capacitive response while the other becomes effectively inductive. Such an electrodynamic imbalance leads to an anomalous negative frequency dispersion regime characterized by the propagation of backward waves. Furthermore, we demonstrate that modifying the dielectric environment or swapping the semiconductor substrate for a metallic one shifts the regions of resonant interaction, offering a versatile means of controlling the spectral intervals of mode splitting. These findings establish a solid theoretical groundwork for the design of tunable nanophotonic devices and the generation of distributed internal feedback, which is essential for the emergence of absolute electromagnetic wave instabilities in beam-coupled systems.

Keywords: *Plasmonic metasurface; Hybrid surface wave; Bulk-surface wave; Negative dispersion; Semiconductor substrate; Mode hybridization*

1. INTRODUCTION

The progress of modern nanophotonics and optoelectronics is largely driven by the search for new ways to manipulate electromagnetic waves at subwavelength scales. In this context, two-dimensional metamaterials—widely known as metasurfaces—have emerged as a focal point of research due to their ability to exhibit electrodynamic properties far beyond those of naturally occurring media [1]. Among these, plasmonic metasurfaces are of particular interest. They offer a versatile toolkit for wave tailoring, supporting extreme field localization, selective routing of surface modes, and fine-tuning of the local density of states. Extensive studies have already uncovered a range of anomalous phenomena linked to their frequency dispersion. It is now a well-recognized fact that these architectures can host tightly confined hybrid electromagnetic states. Typically, the resulting eigenspectrum splits into branches representing hybrid transverse electric (TE) and transverse magnetic (TM) waves [2, 3]. Furthermore, such systems can trigger optical topological transitions, where the isofrequency contours undergo a dynamic transformation from closed ellipses to open hyperbolic curves as the frequency shifts [4]. Accurately modeling these effects requires a precise determination of the effective surface conductivity, often done by merging near-field and far-field characterization methods [5]. A promising direction lies in integrating anisotropic metasurfaces with natural 2D materials like graphene or black phosphorus, or embedding them into multilayered solid-state stacks. For instance, doped 2D layers can support highly directional hyperbolic plasmons, which are easily tuned via electrical gating [6]. It is also worth noting that strong field confinement often arises at the physical boundaries of these anisotropic structures [7]. When multiple metasurfaces are stacked, the interaction between their eigenmodes becomes quite complex. Some theoretical models even compare these coupled modes to Feynman paths in electron transport theory [8]. To evaluate such layered systems, the transfer-matrix formalism remains one of the most reliable and direct analytical tools [9].

Recent research has significantly broadened the known spectrum of guided states. Notable examples include analytical models for anisotropic polarizabilities at arbitrary incidence [10], self-collimated surface-wave steering through equifrequency contour design [11], and the discovery of hybrid waves in twisted metasurfaces [12]. Simultaneously, work on hyperbolic shear metasurfaces [13] and antihyperbolic surface states [14] has opened new routes for controlling mode topology and axial dispersion. Other studies have demonstrated that even isotropic metasurfaces can produce a scattering-free plasmonic Brewster effect for p-polarized waves across a wide range of angles [15]. The strong anisotropy and tunability of these platforms allow for a variety of specialized effects, from near-perfect photon spin selectivity [16] and chiral sensing [17] to quantum-nanophotonic effects in hyperbolic media [18]. Furthermore, the high confinement

Cite as: Yu.O. Averkov, O.Yu. Averkov, N.N. Beletskii, East Eur. J. Phys. 3, 239 (2026), https://doi.org/10.26565/2312-4334-2026-3-19

of surface plasmons enables these systems to exert significant transverse optical forces on nearby nanoparticles [19] or to facilitate directional radiative heat transfer [20]. Practical applications also extend to multiband polarization converters [21], multifunctional polaritonic structures [22], and Babinet-invertible metasurfaces enabling transmission-reflection and helicity switching [23, 24]. However, despite these advances, there is still a lack of comprehensive electrodynamic models for certain asymmetric hybrid architectures. A prime example is a structure where a dielectric layer is placed between a plasmonic metasurface and a semi-infinite plasma-like substrate (such as a metal or semiconductor).

In this paper, we conduct a rigorous theoretical and numerical study of the dispersion properties in such a configuration. Our goal is to identify the conditions for strong wave localization and to analyze the frequency splitting of coupled surface modes in solid-state structures incorporating isotropic plasmonic metasurfaces.

2. PROBLEM STATEMENT

2.1. Main equations and boundary conditions

The physical system under investigation represents a planar, multi-layered solid-state structure. The uppermost region consists of a semi-infinite dielectric superstrate characterized by a permittivity ε_1, which bounds the primary plasmonic metasurface. A dielectric spacer of thickness d_1 and permittivity ε_2 separates this top conductive sheet from a secondary plasmonic metasurface. Beneath this lower structured interface lies another dielectric layer, having a thickness d_2 and permittivity ε_3, which bridges the gap to a semi-infinite plasma-like bulk substrate, typically realized as a highly doped semiconductor or a metal. We orient the z-axis normal to the layer interfaces, defining its positive direction to point into the

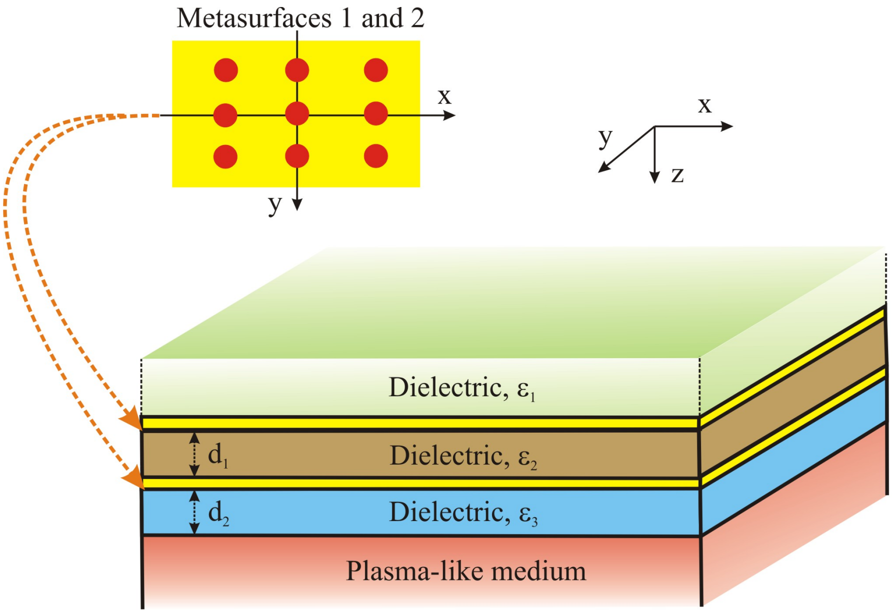

Figure 1. Geometry of the structure.

depth of the plasma-like medium (see Fig. 1). The top metasurface is located precisely at the $z = 0$ plane, while the bottom metasurface is positioned at $z = d_1$. From a physical standpoint, such metasurfaces are typically fabricated as periodic lattices of highly conducting, ultra-thin elements—such as metallic strips or disks. Given that both the thickness of these inclusions and the array periodicity are vastly smaller than the operational wavelength, out-of-plane spatial dispersion becomes entirely negligible. This scale separation permits us to model the electrodynamic behavior of both structured interfaces using macroscopic, isotropic effective surface conductivities, denoted here as σ_1 and σ_2.

The overall field dynamics within this multi-layered geometry are rigorously governed by Maxwell's equations:

$$\nabla \times \mathbf{H}(\mathbf{r}, t) = \frac{1}{c}\frac{\partial \mathbf{D}(\mathbf{r}, t)}{\partial t} + \frac{4\pi}{c}\mathbf{j}(\mathbf{r}, t), \tag{1}$$

$$\nabla \times \mathbf{E}(\mathbf{r}, t) = -\frac{1}{c}\frac{\partial \mathbf{B}(\mathbf{r}, t)}{\partial t}, \tag{2}$$

$$\nabla \cdot \mathbf{D}(\mathbf{r}, t) = 0, \tag{3}$$

$$\nabla \cdot \mathbf{B}(\mathbf{r}, t) = 0. \tag{4}$$

In these expressions, c represents the vacuum speed of light. The variables $\mathbf{E}(\mathbf{r}, t)$, $\mathbf{H}(\mathbf{r}, t)$, and $\mathbf{B}(\mathbf{r}, t)$ correspond to the electric field, magnetic field, and magnetic induction vectors, respectively. Because all constituent layers are assumed to be non-magnetic ($\mu = 1$), the magnetic induction and magnetic fields are strictly equivalent in the Gaussian system, yielding $\mathbf{B}(\mathbf{r}, t) = \mathbf{H}(\mathbf{r}, t)$. The vector $\mathbf{D}(\mathbf{r}, t)$ defines the electric displacement. Additionally, the complete current density within the system is purely planar, taking the form $\mathbf{j}(\mathbf{r},t) = (\mathbf{j}_\tau(\mathbf{r},t), 0)$. This transverse current distribution is mathematically pinned to the patterned interfaces using the Dirac delta function, $\delta(z)$, and can be expanded as $\mathbf{j}_\tau(\mathbf{r},t) = \mathbf{j}_{\tau 1}(\boldsymbol{\rho},t)\delta(z) + \mathbf{j}_{\tau 2}(\boldsymbol{\rho},t)\delta(z-d_1)$, with $\boldsymbol{\rho} = (x,y,0)$ acting as the in-plane position vector.

To analyze the system, we decompose the electromagnetic fields into Fourier integrals of the form [25]:

$$\mathbf{E}(\mathbf{r},t) = \int\limits_{-\infty}^{\infty}\int\limits_{-\infty}^{\infty} \mathbf{E}(\boldsymbol{k},\omega)\exp\left[i(k_z z + \boldsymbol{\kappa\rho} - \omega t)\right] d\boldsymbol{k} d\omega, \tag{5}$$

where ω stands for the angular frequency, and the total wave vector is defined as $\boldsymbol{k} = (\boldsymbol{\kappa}, k_z)$. Its in-plane transverse component is denoted by $\boldsymbol{\kappa} = (k_x, k_y, 0)$, while k_z represents the normal wave number.

Furthermore, the macroscopic constitutive relations coupling the electric displacement to the electric field inherently take a non-local form:

$$D_j(\mathbf{r},t) = \int_{-\infty}^{t} \hat{\varepsilon}_{jg}(t-t')E_g(\mathbf{r},t')dt', \tag{6}$$

where the subscripts j and g designate the Cartesian coordinates (x, y, z), with summation implicitly applied over the index g. The integral kernel $\hat{\varepsilon}_{jg}(t-t')$ serves as the time-domain dielectric response tensor, reflecting the assumption that the electrodynamic properties of the medium are temporally homogeneous. Upon transforming to the frequency domain, this convolution reduces to a straightforward algebraic relation:

$$D_j(\boldsymbol{k},\omega) = \varepsilon_{jg}(\omega)E_g(\boldsymbol{k},\omega). \tag{7}$$

In this formulation, the frequency-domain dielectric tensor $\varepsilon_{jg}(\omega)$ is obtained directly through the Fourier transform of the temporal response kernel:

$$\varepsilon_{jg}(\omega) = \int_{0}^{\infty} \hat{\varepsilon}_{jg}(\tau)\exp(i\omega\tau)d\tau. \tag{8}$$

Inside the purely dielectric regions ($z < 0$, $0 < z < d_1$, and $d_1 < z < d_1 + d_2$), the material response is essentially instantaneous, which is mathematically expressed as $\hat{\varepsilon}_{ij}(\tau) = \varepsilon_m \delta_{ij}\delta(\tau)$. Here, the scalar constant $\varepsilon_m \in \{\varepsilon_1, \varepsilon_2, \varepsilon_3\}$ is assigned according to the specific layer. As a result, the spectral electric displacement reduces to a simple proportionality: $\mathbf{D}_m(\boldsymbol{k},\omega) = \varepsilon_m \mathbf{E}(\boldsymbol{k},\omega)$. In contrast, the plasma-like substrate occupying $z > d_1 + d_2$ exhibits strong temporal dispersion, leading to the relation $\mathbf{D}_4(\boldsymbol{k},\omega) = \varepsilon_4(\omega)\mathbf{E}(\boldsymbol{k},\omega)$, where

$$\varepsilon_4(\omega) = \varepsilon_0 - \frac{\omega_p^2}{\omega(\omega + i\nu)}. \tag{9}$$

In this formulation, ε_0 represents the high-frequency background permittivity, ω_p designates the collective plasma frequency of the free charge carriers, and ν dictates the effective collision rate responsible for intrinsic dissipative losses.

Furthermore, the macroscopic surface currents induced on the patterned interfaces are expressed as:

$$\mathbf{j}_{\tau l}(\boldsymbol{\rho},t) = \int\limits_{-\infty}^{\infty}\int\limits_{-\infty}^{\infty} \mathbf{j}_{\tau l}(\boldsymbol{\kappa},\omega)\exp\left[i(\boldsymbol{\kappa\rho} - \omega t)\right] d\boldsymbol{\kappa} d\omega, \tag{10}$$

where $l \in \{1, 2\}$ indexes the metasurfaces. In the frequency domain, we use:

$$\mathbf{j}_{\tau l}(\boldsymbol{\kappa},\omega) = \sigma_l(\omega)\,\mathbf{E}_\tau(\boldsymbol{\kappa},\omega). \tag{11}$$

Here, the term $\sigma_l(\omega)$ represents the frequency-domain effective surface conductivity of the l-th metasurface, which is mathematically modeled as:

$$\sigma_l(\omega) = \frac{c}{4\pi}\left(\sigma_{\infty l} + \frac{iA_l\omega}{\omega^2 - \Omega_l^2 + i\gamma_l\omega}\right). \tag{12}$$

Here, $\sigma_{\infty l}$ represents the background conductivity arising from deep electronic band transitions ($\mathrm{Re}\,\sigma_{\infty l} = 0$). The amplitude coefficient A_l is determined by the particular subwavelength geometry of the l-th metasurface ($\mathrm{Im}\,A_l = 0$). Additionally, Ω_l denotes the fundamental resonance frequency of the structured layer, while γ_l accounts for the resonance broadening caused by ohmic dissipation and radiation scattering. To focus strictly on the underlying dispersion topology, we hereafter neglect all dissipative mechanisms within both the patterned interfaces and the plasma-like substrate, explicitly setting $\gamma_1 = \gamma_2 = 0$ and $\nu = 0$.

To rigorously extract the dispersion characteristics, we enforce the standard electromagnetic boundary matching at the three primary interfaces ($z = 0$, $z = d_1$, and $z = d_1 + d_2$). At the metasurface planes located at $z = 0$ and $z = d_1$, the tangential electric field remains strictly continuous. In contrast, the tangential magnetic field undergoes a discrete discontinuity driven by the localized surface currents:

$$\mathbf{n}\times\Big(\mathbf{E}_{m+1}(\mathbf{r},t)-\mathbf{E}_m(\mathbf{r},t)\Big)=0, \tag{13}$$

$$\mathbf{n}\times\Big(\mathbf{H}_{m+1}(\mathbf{r},t)-\mathbf{H}_m(\mathbf{r},t)\Big)=\frac{4\pi}{c}\mathbf{j}_{\tau l}(\boldsymbol{\rho},t). \tag{14}$$

In this notation, $\mathbf{n}=(0,0,1)$ represents the unit normal vector pointing from the m-th medium into the $(m+1)$-th medium, where the index $m\in\{1,2\}$ specifies the dielectric domains immediately bounding the l-th metasurface. Furthermore, since the boundary separating the bottom dielectric spacer and the plasma-like substrate (located at $z=d_1+d_2$) lacks any conducting inclusions, it cannot support free surface currents. Consequently, both the tangential electric and magnetic field components transition continuously across this final interface:

$$\mathbf{n}\times\Big(\mathbf{E}_4(\mathbf{r},t)-\mathbf{E}_3(\mathbf{r},t)\Big)=0,\quad \mathbf{n}\times\Big(\mathbf{H}_4(\mathbf{r},t)-\mathbf{H}_3(\mathbf{r},t)\Big)=0. \tag{15}$$

2.2. Dispersion relations of structure eigenwaves

To derive the dispersion relations for the p-polarized (transverse magnetic) eigenmodes supported by the proposed structure, we first specify the relevant electromagnetic field vectors. Under this polarization scheme, the fields exhibit the non-vanishing components $\mathbf{E}(\boldsymbol{r},t)=(E_x(\boldsymbol{r},t),0,E_z(\boldsymbol{r},t))$ and $\mathbf{H}(\boldsymbol{r},t)=(0,H_y(\boldsymbol{r},t),0)$. Assuming unidirectional wave propagation strictly along the x-axis, the associated wave vector simplifies to $\boldsymbol{k}=(k_x,0,k_z)$.

Applying this specific spatial field configuration requires us to adapt the general macroscopic boundary conditions across all structural interfaces. Specifically, evaluating these matching conditions at the plane containing the top metasurface ($z=0$) yields:

$$E_{x2}(x,t)\Big|_{z=0}=E_{x1}(x,t)\Big|_{z=0}, \tag{16}$$

$$H_{y2}(x,t)\Big|_{z=0}-H_{y1}(x,t)\Big|_{z=0}=-\frac{4\pi}{c}j_{\tau1,x}(\boldsymbol{\rho},t)\Big|_{z=0}. \tag{17}$$

At the plane of the second metasurface ($z=d_1$):

$$E_{x3}(x,t)\Big|_{z=d_1}=E_{x2}(x,t)\Big|_{z=d_1}, \tag{18}$$

$$H_{y3}(x,t)\Big|_{z=d_1}-H_{y2}(x,t)\Big|_{z=d_1}=-\frac{4\pi}{c}j_{\tau2,x}(\boldsymbol{\rho},t)\Big|_{z=d_1}. \tag{19}$$

At the interface between dielectric 3 and the plasma-like medium ($z=d_1+d_2$):

$$E_{x4}(x,t)\Big|_{z=d_1+d_2}=E_{x3}(x,t)\Big|_{z=d_1+d_2}, \tag{20}$$

$$H_{y4}(x,t)\Big|_{z=d_1+d_2}=H_{y3}(x,t)\Big|_{z=d_1+d_2}. \tag{21}$$

We first deduce the dispersion relation specific to the *surface eigenwaves* of the structure. Moving forward, the relevant spatial and frequency parameters are expressed in dimensionless form, normalized with respect to the fundamental resonant frequency of the first metasurface, Ω_1:

$$\xi=\frac{\omega}{\Omega_1},\ q=\frac{ck_x}{\Omega_1},\ \delta_1=\frac{d_1\Omega_1}{c},\ \delta_2=\frac{d_2\Omega_1}{c}. \tag{22}$$

The dimensionless transverse decay constants in the corresponding layers are defined as:

$$\eta_m=i\frac{ck_{zm}}{\Omega_1}=\sqrt{q^2-\xi^2\varepsilon_m}\quad(m=1,2,3),\ \eta_4=i\frac{ck_{z4}}{\Omega_1}=\sqrt{q^2-\xi^2\varepsilon_4(\xi)}. \tag{23}$$

The remaining normalized physical parameters of the materials are given by:

$$\bar{\omega}_p=\frac{\omega_p}{\Omega_1},\ \xi_2=\frac{\Omega_2}{\Omega_1},\ \bar{A}_l=\frac{A_l}{\Omega_1},\ \bar{\sigma}_{\infty l}=-\frac{4\pi i}{c}\sigma_{\infty l}, \tag{24}$$

where the index $l\in\{1,2\}$ refers to the first and second metasurface, respectively.

In terms of these newly defined variables, the Fourier-transformed permittivity of the plasma-like medium and the effective surface conductivities reduce to the following expressions:

$$\varepsilon_4(\xi) = \varepsilon_0 - \frac{\bar{\omega}_p^2}{\xi^2},\ \bar{\sigma}_1(\xi) = -\frac{4\pi i}{c}\sigma_1(\omega) = \bar{\sigma}_{\infty 1} + \frac{\bar{A}_1\xi}{\xi^2 - 1}, \tag{25}$$

$$\bar{\sigma}_2(\xi) = -\frac{4\pi i}{c}\sigma_2(\omega) = \bar{\sigma}_{\infty 2} + \frac{\bar{A}_2\xi}{\xi^2 - \xi_2^2}. \tag{26}$$

By substituting the integral representations of the fields (5) and the surface currents (10) into the boundary conditions (16)–(21), we arrive at the dispersion relation governing the *surface eigenwaves*:

$$a_1\left[\frac{b_3}{b_1} - \frac{b_4}{b_2}\exp(-2\eta_2\delta_1)\right]\exp(-2\eta_3\delta_2) + a_2\left[\frac{b_6}{b_1} - \frac{b_5}{b_2}\exp(-2\eta_2\delta_1)\right] = 0, \tag{27}$$

where

$$a_1 = \frac{\varepsilon_4}{\eta_4} - \frac{\varepsilon_3}{\eta_3},\ a_2 = \frac{\varepsilon_4}{\eta_4} + \frac{\varepsilon_3}{\eta_3}, \tag{28}$$

$$b_1 = \left(\frac{\varepsilon_1}{\eta_1} - \frac{\varepsilon_2}{\eta_2}\right)\xi - \bar{\sigma}_1(\xi),\ b_2 = \left(\frac{\varepsilon_1}{\eta_1} + \frac{\varepsilon_2}{\eta_2}\right)\xi - \bar{\sigma}_1(\xi),\ b_3 = \left(\frac{\varepsilon_3}{\eta_3} - \frac{\varepsilon_2}{\eta_2}\right)\xi + \bar{\sigma}_2(\xi), \tag{29}$$

$$b_4 = \left(\frac{\varepsilon_3}{\eta_3} + \frac{\varepsilon_2}{\eta_2}\right)\xi + \bar{\sigma}_2(\xi),\ b_5 = \left(\frac{\varepsilon_3}{\eta_3} - \frac{\varepsilon_2}{\eta_2}\right)\xi - \bar{\sigma}_2(\xi),\ b_6 = \left(\frac{\varepsilon_3}{\eta_3} + \frac{\varepsilon_2}{\eta_2}\right)\xi - \bar{\sigma}_2(\xi). \tag{30}$$

As the thickness δ_2 tends toward infinity, the composite dispersion relation (27) decouples into two independent equations. These specifically describe the eigenmodes of the dielectric 3–plasma-like interface and the isolated five-layer metasurface structure (dielectric 1–metasurface 1–dielectric 2–metasurface 2–dielectric 3), respectively:

$$\frac{\varepsilon_4}{\eta_4} + \frac{\varepsilon_3}{\eta_3} = 0,\ \frac{b_6}{b_1} - \frac{b_5}{b_2}\exp(-2\eta_2\delta_1) = 0. \tag{31}$$

Next, we focus on the *bulk-surface eigenwaves*, which are characterized by fields that exhibit exponential decay (evanescence) within the top dielectric and the semiconductor substrate, while maintaining an oscillatory profile inside the internal dielectric spacers 2 and 3. This specific waveguiding regime is supported when the following phase-matching conditions are satisfied: $q^2 > \xi^2\varepsilon_1$, $q^2 > \xi^2\varepsilon_4(\xi)$, $q^2 < \xi^2\varepsilon_2$, and $q^2 < \xi^2\varepsilon_3$. We will use the following notation for the normal components of the wave vector in dielectrics 2 and 3:

$$\zeta_2 = \sqrt{\xi^2\varepsilon_2 - q^2}, \quad \zeta_3 = \sqrt{\xi^2\varepsilon_3 - q^2}. \tag{32}$$

The dispersion relation governing the bulk-surface waves is derived from Eq. (27) by enforcing an oscillatory field profile within the internal dielectric spacers (layers 2 and 3). This transition is mathematically handled by substituting the transverse decay constants with their purely imaginary counterparts, $\eta_2 = -i\zeta_2$ and $\eta_3 = -i\zeta_3$. By subsequently invoking Euler's identities to recast the complex exponentials into a trigonometric form, we arrive at the following expression:

$$\begin{aligned}&\cos(\varphi_1)\left\{\xi\left(\frac{\varepsilon_3}{\zeta_3} - \frac{\varepsilon_2}{\zeta_2}\right)\left[\xi\left(\frac{\varepsilon_2}{\zeta_2}\Delta_1 - \frac{\varepsilon_1}{\eta_1}\Delta_2\right) + \bar{\sigma}_1(\xi)\Delta_2\right] - \bar{\sigma}_2(\xi)\left[\xi\left(\frac{\varepsilon_1}{\eta_1}\Delta_1 + \frac{\varepsilon_2}{\zeta_2}\Delta_2\right) - \bar{\sigma}_1(\xi)\Delta_1\right]\right\}\\ &+ \cos(\varphi_2)\left\{\xi\left(\frac{\varepsilon_3}{\zeta_3} + \frac{\varepsilon_2}{\zeta_2}\right)\left[\xi\left(\frac{\varepsilon_1}{\eta_1}\Delta_3 + \frac{\varepsilon_2}{\zeta_2}\Delta_4\right) - \bar{\sigma}_1(\xi)\Delta_3\right] + \bar{\sigma}_2(\xi)\left[\xi\left(\frac{\varepsilon_1}{\eta_1}\Delta_4 - \frac{\varepsilon_2}{\zeta_2}\Delta_3\right) - \bar{\sigma}_1(\xi)\Delta_4\right]\right\} = 0,\end{aligned} \tag{33}$$

where

$$\Delta_1 = \frac{\varepsilon_4}{\eta_4} - \frac{\varepsilon_3}{\zeta_3}\tan(\varphi_1),\ \Delta_2 = \frac{\varepsilon_3}{\zeta_3} + \frac{\varepsilon_4}{\eta_4}\tan(\varphi_1),\ \Delta_3 = \frac{\varepsilon_3}{\zeta_3} - \frac{\varepsilon_4}{\eta_4}\tan(\varphi_2),\ \Delta_4 = \frac{\varepsilon_4}{\eta_4} + \frac{\varepsilon_3}{\zeta_3}\tan(\varphi_2), \tag{34}$$

$$\varphi_1 = \zeta_2\delta_1 - \zeta_3\delta_2,\ \varphi_2 = \zeta_2\delta_1 + \zeta_3\delta_2. \tag{35}$$

We also examine a specific class of *bulk-surface eigenwaves* characterized by evanescent field profiles in the vacuum cladding, the first dielectric spacer, and the plasma-like substrate, while sustaining an oscillatory behavior strictly within the third dielectric layer. These modes are supported when the in-plane wave number q satisfies the phase-matching inequalities $q^2 > \xi^2\varepsilon_1$, $q^2 > \xi^2\varepsilon_2$, and $q^2 > \xi^2\varepsilon_4(\xi)$, but remains below the light line of the silica layer ($q^2 < \xi^2\varepsilon_3$). Under these conditions, the governing dispersion equation takes the following form:

$$g\frac{\varepsilon_4}{\eta_4} - f\frac{\varepsilon_3}{\zeta_3} + \left(g\frac{\varepsilon_3}{\zeta_3} + f\frac{\varepsilon_4}{\eta_4}\right)\tan(\zeta_3\delta_2) = 0, \tag{36}$$

where

$$f = -\xi\frac{\varepsilon_2}{\eta_2}\left[\frac{1}{b_1} + \frac{1}{b_2}\exp(-2\eta_2\delta_1)\right] + \bar{\sigma}_2(\xi)\left[\frac{1}{b_1} - \frac{1}{b_2}\exp(-2\eta_2\delta_1)\right], \tag{37}$$

$$g = \xi\frac{\varepsilon_3}{\zeta_3}\left[\frac{1}{b_1} - \frac{1}{b_2}\exp(-2\eta_2\delta_1)\right]. \tag{38}$$

3. NUMERICAL ANALYSIS OF DISPERSION RELATIONS

To numerically evaluate the dispersion profiles, we adopt the following material parameters: vacuum for the top layer ($\varepsilon_1 = 1$), Teflon for the first spacer ($\varepsilon_2 = 2.1$), fused silica for the second spacer ($\varepsilon_3 = 3.7$), and an InSb semiconductor substrate ($\varepsilon_0 = 15.68$). The normalized geometric and metasurface parameters are fixed at $\bar{\sigma}_{\infty 1} = \bar{\sigma}_{\infty 2} = 0.2$, $\bar{A}_1 = \bar{A}_2 = 0.2$, $\delta_1 = 0.3$, $\delta_2 = 0.15$, and $\xi_2 = 1.3$. In the subsequent analysis, only the dimensionless plasma frequency $\bar{\omega}_p$ and the oscillator strengths $\bar{A}_l$ will be treated as variable quantities.

Our numerical analysis relies on a fundamental physical concept: pronounced branch repulsion—typically referred to as an avoided crossing—emerges whenever the eigenfrequencies of initially non-degenerate modes approach one another. The proposed six-layer structure inherently supports three distinct resonant states: the fundamental resonance of the top metasurface ($\xi_1 = 1$), the resonance of the bottom metasurface (ξ_2), and the surface plasmon-polariton (SPP) supported by the boundary between the semiconductor substrate and the adjacent silica spacer. This SPP resonance is governed by the standard matching condition $\varepsilon_4 + \varepsilon_3 = 0$.

We aim to track how the overall mode spectrum reorganizes as the normalized SPP frequency, defined as $\xi_{sp} = \bar{\omega}_p/\sqrt{\varepsilon_0 + \varepsilon_3}$, is systematically swept across the metasurface resonances, specifically moving from a sub-resonant regime ($\xi_{sp} < \xi_1$) to a supra-resonant one ($\xi_{sp} > \xi_2$, assuming $\xi_2 > \xi_1$).

We start by examining a scenario where the SPP frequency resides well below the resonant frequencies of both structured layers, meaning $\xi_{sp} < \xi_1 < \xi_2$. The resulting eigenspectrum under these conditions is plotted in Fig. 2, calculated for $\bar{\omega}_p = 3.5$ and identical oscillator strengths $\bar{A}_1 = \bar{A}_2 = 0.2$.

To ensure consistency across all spectra of electromagnetic waves (Figs. 2, 4–8), we use a unified labeling scheme. The straight lines denoted by 1, 2, and 3 are the light lines corresponding to the vacuum, Teflon, and silica regions, respectively. Curve 4 marks the transition boundary where the transverse decay constant inside the semiconductor vanishes ($\eta_4 = 0$). The horizontal lines 5 and 6 specify the isolated resonant frequencies of the upper ($\xi_1 = 1$) and lower ($\xi_2 = 1.3$) metasurfaces, while line 7 tracks the SPP frequency ξ_{sp}. Furthermore, the lower-frequency and upper-frequency dispersion branches originating from the metasurfaces are identified as curves 8, 9 and 11, 12. Finally, curve 10 specifically maps the electromagnetic state that remains largely confined to the semiconductor interface. In Fig. 9, lines 1–3 have the same meaning as in the preceding figures; line 4 corresponds to $\xi_1 = 1$, line 5 to $\xi_2 = 1.3$, and line 6 to ξ_{sp}. Curves 7, 8 and 10, 11 represent, respectively, the low-frequency and high-frequency branches of electromagnetic waves predominantly localized near the metasurfaces, whereas curve 9 represents an electromagnetic wave predominantly localized near the plasma-like medium.

As illustrated in Fig. 2, the dispersion branches representing the low-frequency ($\xi < 1$) modes largely confined to the two metasurfaces (curves 8 and 9) exhibit a clear avoided crossing within region B. This repulsion signifies a strong

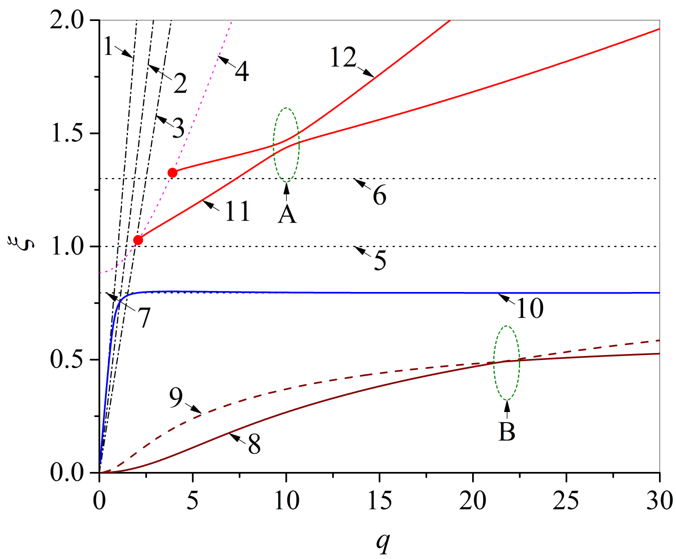

Figure 2. Dispersion spectrum of electromagnetic waves in the analyzed solid-state structure when $\xi_{sp} < \xi_1 < \xi_2$ (with $\bar{\omega}_p = 3.5$). The highlighted areas A and B demonstrate the pronounced resonant coupling between the underlying non-degenerate modes.

resonant coupling between the initially non-degenerate states. The higher-frequency ($\xi > 1$) metasurface modes undergo a comparable hybridization process. Specifically, in region A, dispersion curves 11 and 12—which correspond to the electromagnetic states governed by the upper and lower metasurfaces—mutually repel and diverge. Because we have set $\xi_{sp} < \xi_1 = 1$, the branch principally confined to the semiconductor substrate (curve 10) remains entirely uncoupled from the upper-frequency metasurface branches. Instead, the primary energy exchange in this high-frequency domain occurs exclusively between the two metasurfaces themselves, driving the pronounced splitting observed in region A. Notably, both curves 11 and 12 originate from the boundary defined by curve 4. At wave numbers below this threshold, the electromagnetic fields inside the semiconductor adopt an oscillatory character, precluding the existence of purely bound surface wave solutions. Furthermore, as curve 10 crosses the relevant light lines, its physical nature transitions. The segment bounded by spectral lines 1 and 2 captures a bulk-surface wave governed by Eq. (33), whereas the section between light lines 2 and 3 maps to a distinct bulk-surface state accurately described by Eq. (36).

We now turn our attention to the specific shape of curve 10 from Fig. 2 and its dependence on the structural oscillator strengths, $\bar{A}_1$ and $\bar{A}_2$. To isolate this effect, Fig. 3 plots the dispersion profile of the semiconductor-confined mode under the exact same background parameters, leaving only the conductivity amplitudes $\bar{A}_1$ and $\bar{A}_2$ as variable quantities.

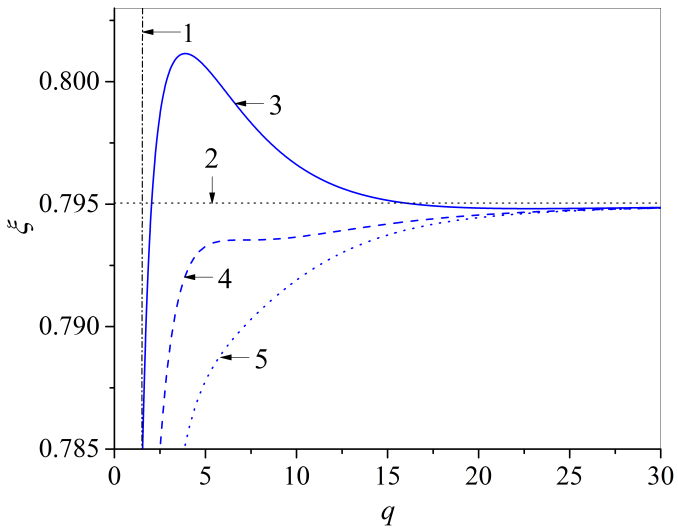

Figure 3. Dispersion spectrum of the electromagnetic mode confined near the plasma-like substrate. The structural parameters match those in Fig. 2, evaluated for oscillator strengths $\bar{A}_1 = \bar{A}_2 = 0.2$ (curve 3), $\bar{A}_1 = \bar{A}_2 = 0.4$ (curve 4), and $\bar{A}_1 = \bar{A}_2 = 0.6$ (curve 5). Line 1 denotes the light line in the third dielectric layer, while line 2 indicates the surface plasmon-polariton (SPP) resonance at $\xi_{sp} \approx 0.8$.

As depicted in Fig. 3, setting the oscillator strengths to $\bar{A}_1 = \bar{A}_2 = 0.2$ induces a distinct anomalous segment characterized by negative dispersion on the branch associated with the semiconductor-confined mode. Within this specific frequency band, the electrodynamic parameters satisfy the following criteria: $\varepsilon_4 < 0$, $\bar{\sigma}_1(\xi) = -4\pi i\sigma_1(\xi)/c < 0$, and $\bar{\sigma}_2(\xi) = -4\pi i\sigma_2(\xi)/c > 0$. Conversely, increasing these oscillator strengths to $\bar{A}_1 = \bar{A}_2 = 0.4$ (curve 4) or $\bar{A}_1 = \bar{A}_2 = 0.6$ (curve 5) completely eliminates the backward-wave behavior. Under these higher-strength conditions, the system enters a regime where both patterned layers share an identical reactive nature, meaning that $\varepsilon_4 < 0$, $\bar{\sigma}_1(\xi) = -4\pi i\sigma_1(\xi)/c < 0$, and crucially, $\bar{\sigma}_2(\xi) = -4\pi i\sigma_2(\xi)/c < 0$ across the entirety of curves 4 and 5.

This analysis demonstrates that for a specific subset of parameters $\bar{A}_1$ and $\bar{A}_2$, a profound electrodynamic asymmetry is established within the stack. Specifically, the top metasurface maintains a fundamentally capacitive profile ($-4\pi i\sigma_1(\xi)/c < 0$), whereas the bottom metasurface transitions to an inductive, metal-like behavior ($-4\pi i\sigma_2(\xi)/c > 0$). It is precisely this competitive capacitive-inductive feedback between the adjacent structured layers that drives the emergence of the negative-dispersion region. From a practical standpoint, the generation of such a backward-wave segment provides the internal distributed feedback necessary to support absolute instabilities when the hybrid geometry is coupled to a synchronized beam of charged particles.

Let us consider the case where the SPP frequency practically coincides with the resonance frequency of the first metasurface, i.e.,

$$\xi_{sp} \approx \xi_1 = 1 < \xi_2 = 1.3.$$

The corresponding eigenspectrum is shown in Fig. 4 for $\bar{\omega}_p = 4.4$ and $\bar{A}_1 = \bar{A}_2 = 0.2$. Due to the frequency degeneracy ($\xi_{sp} \approx \xi_1 = 1$), a regime of strong mode hybridization is achieved. This leads to a pronounced anticrossing (curve repulsion), highlighted as Region A, between curve 10, which corresponds to the mode predominantly localized near the plasma-like medium, and curve 11, the high-frequency branch predominantly associated with metasurface 1. The strong electrodynamic coupling fundamentally reorganizes the spectrum in the vicinity of $\xi = 1$. Additionally, Regions B and C indicate the secondary resonant interactions between the high-frequency and low-frequency electromagnetic waves, respectively, which are localized near the two separated metasurfaces.

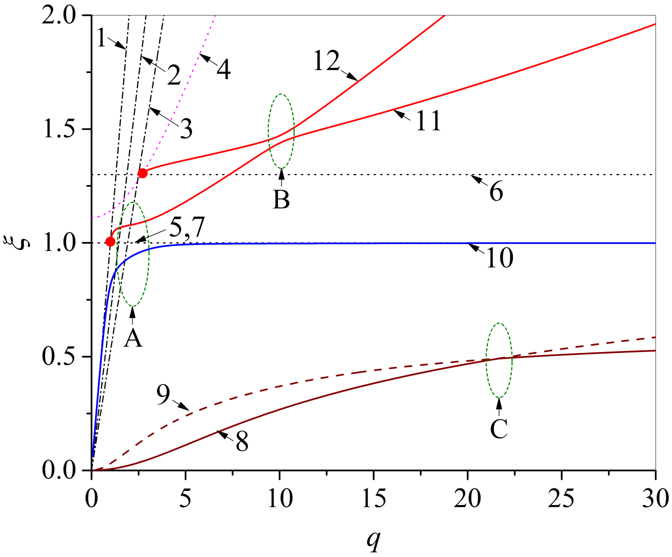

Figure 4. Dispersion spectrum of electromagnetic waves in the analyzed solid-state structure under the condition $\xi_{sp} \approx \xi_1 = 1 < \xi_2 = 1.3$ (where $\bar{\omega}_p = 4.4$). Region A features a substantial avoided crossing between the dispersion branch of the plasma-like medium (curve 10) and that of the primary metasurface (curve 11).

Fig. 5 demonstrates the eigenspectrum for a uniform distribution of resonances, where $\xi_1 = 1 < \xi_{sp} \approx 1.13 < \xi_2 = 1.3$ (with $\bar{\omega}_p = 5.0$).

In this regime, the system avoids giant single-point mode splitting and instead forms a characteristic "ladder" of repelling branches. The spectrum features three distinct interaction areas: Region A corresponds to the coupling of the proper high-frequency surface modes localized near both metasurfaces; Region B highlights the interaction between the branch localized near metasurface 1 and the branch predominantly localized near the plasma-like medium (curve 10); and Region C reflects the mutual coupling of the low-frequency metasurface modes. Such a sequential repulsion mechanism reveals the complex cascaded nature of the mode interactions across the entire structure. Therefore, when the SPP frequency falls between the two metasurface resonances, the spectrum undergoes a sequential reorganization. It starts with the hybridization of low-frequency modes, followed by the interaction between the plasma-like branch and the first metasurface branch, and culminates in the mutual repulsion of the high-frequency branches.

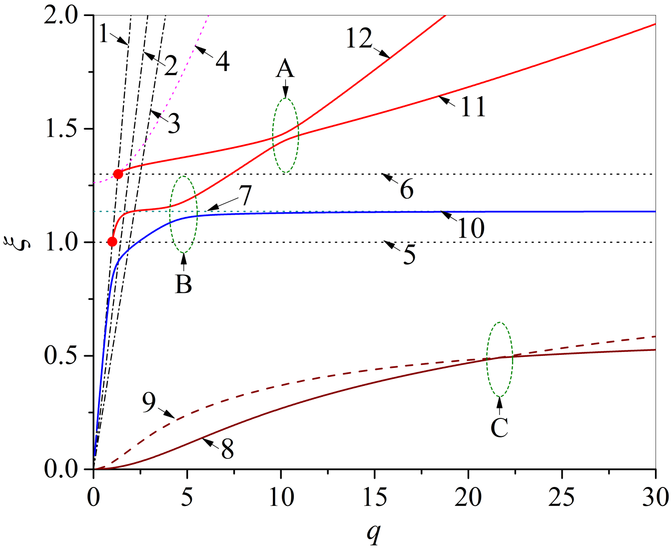

Figure 5. Dispersion spectrum of electromagnetic waves in the analyzed solid-state structure for an evenly spaced arrangement of resonances, taking $\xi_1 = 1 < \xi_{sp} \approx 1.13 < \xi_2 = 1.3$ ($\bar{\omega}_p = 5.0$). A distinct sequence, or "ladder," of mutually repelling dispersion branches emerges across interaction zones A, B, and C.

Ultimately, we examine the scenario where the SPP frequency nears the resonant frequency of the second metasurface, given by $\xi_1 = 1 < \xi_{sp} \approx \xi_2 = 1.3$.

Fig. 6 illustrates the resulting dispersion profile for $\bar{\omega}_p = 5.7$. Under these conditions, the primary avoided crossing moves to a higher frequency range, taking place between curve 10—representing the mode largely confined to the plasma-like semiconductor—and curve 12, which represents the upper-frequency mode principally linked to the second metasurface. Consequently, a substantial spectral gap emerges in region C around $\xi = 1.3$. Furthermore, region A continues to capture the coupling between the two intrinsic upper-frequency metasurface modes, while region B highlights the interaction linking the plasma-like-medium branch with the branch governed by the first metasurface. In the lower-frequency spectrum, region D indicates the ongoing mutual repulsion of the bottom-tier metasurface branches. Therefore, as ξ_{sp} transitions away from ξ_1 and closer to ξ_2, the primary pathway for energy hybridization shifts from the first metasurface to the second. Concurrently, the preservation of the other interaction zones clearly underscores the fundamentally multiresonant nature of this six-layer structure.

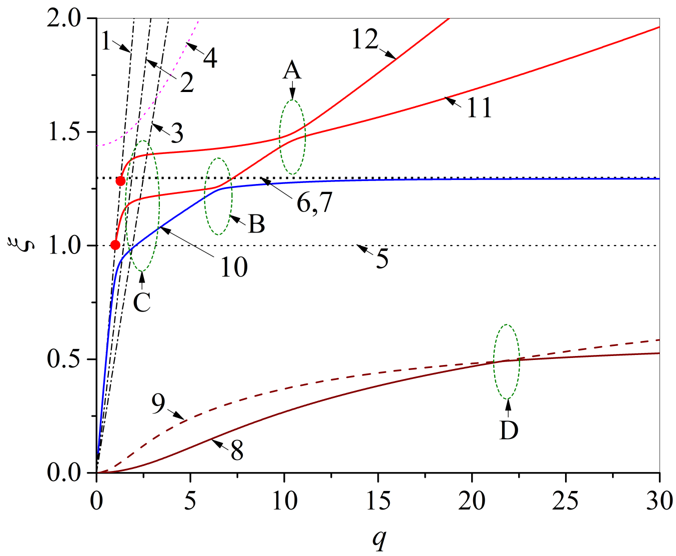

Figure 6. Dispersion spectrum of electromagnetic waves in the analyzed solid-state structure under the condition $\xi_1 = 1 < \xi_{sp} \approx 1.3 \approx \xi_2$ (with $\bar{\omega}_p = 5.7$). The most significant mode hybridization and splitting are localized within Region C.

To evaluate the impact of the dielectric environment, we consider the case where the fused-silica spacer is replaced by a high-index silicon layer ($\varepsilon_3 = 11.7$). As shown in Fig. 7, the increased permittivity causes the light line in the third dielectric (curve 3) to shift downward. This modification, combined with the high background permittivity of the semiconductor, reduces the SPP frequency to $\xi_{sp} \approx 0.95$. Consequently, the SPP resonance resides below the primary metasurface resonance ($\xi_{sp} < \xi_1$), which prevents the splitting of the semiconductor-localized branch (curve 10) through interaction with the metasurface modes. However, the intrinsic coupling between the two metasurfaces remains active, leading to the pronounced avoided crossing observed in Region A for the high-frequency branches.

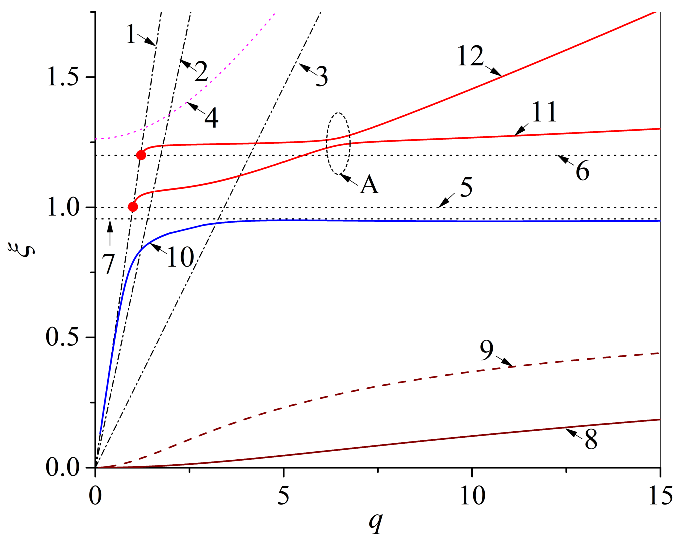

Figure 7. Dispersion spectrum of electromagnetic waves in the analyzed solid-state structure with a high-index dielectric spacer (silicon, $\varepsilon_3 = 11.7$) for the case $\xi_{sp} \approx 0.95 < \xi_1 = 1 < \xi_2 = 1.3$ ($\bar{\omega}_p = 5.0$). Curves 1, 2, and 3 represent light lines; curve 4 marks the boundary $\eta_4 = 0$; lines 5, 6, and 7 indicate ξ_1, ξ_2, and ξ_{sp}, respectively. Curves 8–12 identify the low- and high-frequency hybrid branches.

The influence of the metasurface oscillator strengths on the hybridization width is illustrated in Fig. 8. By increasing the parameters $\bar{A}_1$ and $\bar{A}_2$ from 0.2 to 0.4 while maintaining other system variables, we observe a significant expansion of the spectral gaps. The anti-crossing regions A, B, and C become notably wider. In this configuration, Region A characterizes the interaction between the upper-frequency metasurface modes, while Region B represents the coupling between the primary metasurface and the plasma-like substrate. Region C captures the repulsion between the fundamental low-frequency metasurface branches. This demonstrates that the geometric design of the conductive elements provides a robust mechanism for controlling the magnitude of mode splitting.

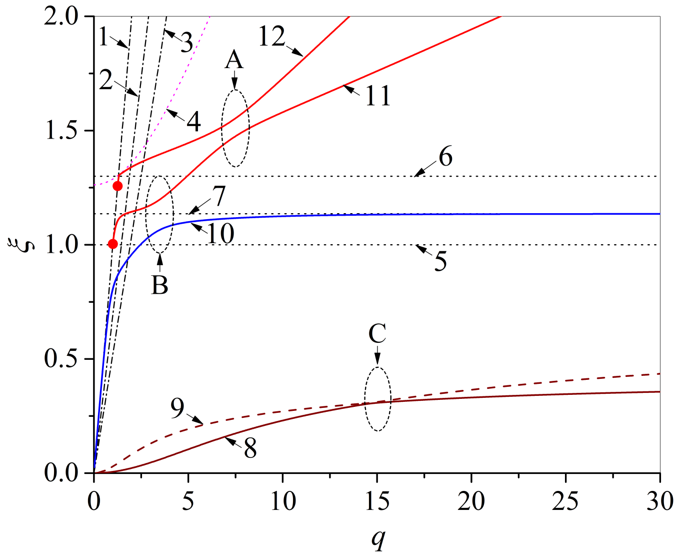

Figure 8. Dispersion spectrum of electromagnetic waves in the analyzed solid-state structure under strong coupling conditions, where the oscillator strengths are increased to $\bar{A}_1 = \bar{A}_2 = 0.4$ ($\bar{\omega}_p = 5.0$, $\xi_{sp} \approx 1.13$). The labeling of branches 1–12 follows the scheme established in Fig. 7.

Finally, we examine the transition from a semiconductor-like to a metal-like substrate by setting the background permittivity to $\varepsilon_0 = 1$. As seen in Fig. 9, this shift dramatically increases the SPP resonance frequency to $\xi_{sp} \approx 2.3$. A comparison between Fig. 8 and Fig. 9 reveals that the metallic nature of the substrate introduces a new interaction zone, labeled Region D, where the SPP branch of the substrate couples strongly with the mode localized near the second metasurface. Furthermore, the existing interaction regions A and B are shifted toward the higher-frequency domain. We also observe that the spectral repulsion between the low-frequency metasurface branches (Region C) is significantly enhanced compared to the semiconductor-based configuration.

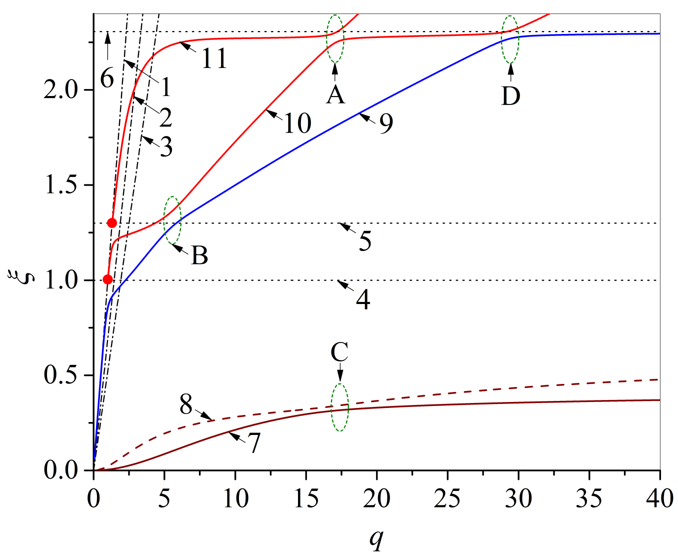

Figure 9. Dispersion spectrum of electromagnetic waves in the analyzed solid-state structure with a metal-like plasma medium ($\varepsilon_0 = 1$) at $\xi_{sp} \approx 2.3 > \xi_2 > \xi_1$. The parameters are $\bar{A}_1 = \bar{A}_2 = 0.4$ and $\delta_1 = \delta_2 = 0.15$. Region D highlights the additional interaction zone emerging at the SPP frequency.

4. DISCUSSION AND CONCLUSION

Our study presents a detailed electrodynamic account of a six-layer hybrid structure, where two isotropic plasmonic metasurfaces are integrated within dielectric spacers above a semi-infinite plasma-like medium. By analyzing the dispersion relations for p-polarized electromagnetic waves, we have mapped a variety of waveguiding regimes. These range from tightly confined surface states to hybrid bulk-surface modes, where the fields exhibit an oscillatory character within the internal dielectrics while maintaining evanescent decay in the cladding and substrate. Numerical results highlight the decisive role of cascaded mode hybridization in shaping the structure's response. Specifically, we found that tuning the surface plasmon-polariton (SPP) frequency of the substrate relative to the metasurfaces' inherent resonances triggers a complex topological reorganization of the eigenspectrum. The strong repulsion between initially non-degenerate states manifests as a multi-resonant "ladder" of dispersion branches. Notably, the spectral position and width of these hybridization gaps prove to be highly sensitive to both the geometric dimensions and the material parameters of the stack. One of the central findings of this work is the identification of the specific parameters necessary for a backward-wave regime. We demonstrated that by introducing an asymmetry in the effective oscillator strengths of the structured interfaces, the system can be forced into a state of competitive reactive feedback. In this specific configuration, the top metasurface remains fundamentally capacitive ($-4\pi i\sigma_1(\xi)/c < 0$), whereas the lower one transitions into a metallic, inductive state ($-4\pi i\sigma_2(\xi)/c > 0$). This electrodynamic imbalance serves as the direct physical mechanism behind the emergence of negative dispersion. From a practical standpoint, creating such intrinsic distributed feedback is essential for triggering absolute instabilities during interactions with synchronized charged-particle beams. Finally, our analysis shows that the energy exchange pathways can be fundamentally shifted by modifying the local dielectric environment or replacing the semiconductor with a metal. Such adjustments alter the critical SPP frequency, effectively pushing the primary interaction zones into higher frequency domains and broadening the spectral gaps between the lowest-order branches. This structural flexibility offers a predictable and versatile platform for managing subwavelength electromagnetic confinement, which is crucial for the next generation of active optoelectronic and nanophotonic devices.

ORCID

Yu.O. Averkov, https://orcid.org/0000-0002-1169-9393; **O.Yu. Averkov**, https://orcid.org/0000-0001-6055-015X; **N.N. Beletskii**, https://orcid.org/0000-0002-3194-7251

REFERENCES

[1] A. Ranjbar and A. Grbic, "Broadband, Multiband, and Multifunctional All-Dielectric Metasurfaces," Phys. Rev. Applied, **11**, 054066 (2019). https://doi.org/10.1103/PhysRevApplied.11.054066

[2] D. Correas-Serrano, J. S. Gomez-Diaz, A. Alvarez-Melcon, and A. Alù, "Black phosphorus plasmonics: anisotropic elliptical propagation and nonlocality-induced canalization," J. Opt. **18**, 104006 (2016). https://doi.org/10.1088/2040-8978/18/10/104006

[3] J. S. Gomez-Diaz, M. Tymchenko, and A. Alù, "Hyperbolic Plasmons and Topological Transitions Over Uniaxial Metasurfaces," Phys. Rev. Lett. **114**, 233901 (2015). https://doi.org/10.1103/PhysRevLett.114.233901

[4] A. A. High, R. C. Devlin, A. Dibos, M. Polking, D. S. Wild, J. Perczel, N. P. de Leon, M. D. Lukin, and H. Park, "Visible-frequency hyperbolic metasurface," Nature, **522**, 192–196 (2015). https://doi.org/10.1038/nature14477

[5] C. L. Holloway, E. F. Kuester, J. A. Gordon, J. O'Hara, J. Booth, and D. R. Smith, "An overview of the theory and applications of metasurfaces: The two-dimensional equivalents of metamaterials," IEEE Antennas Propag. Mag. **54**, 10–35 (2012). https://doi.org/10.1109/MAP.2012.6230714

[6] A. Nemilentsau, T. Low, and G. Hanson, "Anisotropic 2D Materials for Tunable Hyperbolic Plasmonics," Phys. Rev. Lett. **116**, 066804 (2016). https://doi.org/10.1103/PhysRevLett.116.066804

[7] P. A. D. Gonçalves, L. P. Bertelsen, S. Xiao, and N. A. Mortensen, "Hybridized Plasmons in 2D Nanoslits: From Graphene to Anisotropic 2D Materials," ACS Photonics, **4**, 2645–2652 (2017). https://doi.org/10.1021/acsphotonics.7b00558

[8] J. Sperrhake, M. Falkner, S. Fasold, T. Kaiser, and T. Pertsch, "Equivalence of reflection paths of light and Feynman paths in stacked metasurfaces," Phys. Rev. B, **102**, 245108 (2020). https://doi.org/10.1103/PhysRevB.102.245108

[9] T. Zhan, X. Shi, Y. Dai, X. Liu, and J. Zi, "Transfer matrix method for optics in graphene layers," J. Phys.: Condens. Matter, **25**, 215301 (2013). https://doi.org/10.1088/0953-8984/25/21/215301

[10] I. Allayarov, V. R. Tuz, A. Cala Lesina, and A. B. Evlyukhin, "Analytical model of metasurfaces comprising meta-atoms with anisotropic polarizabilities and for arbitrary incident angles," Phys. Rev. B, **111**, 155438 (2025). https://doi.org/10.1103/PhysRevB.111.155438

[11] S. M. Kandil, D. J. Bisharat, and D. F. Sievenpiper, "Engineering equifrequency contours of metasurfaces for self-collimated surface-wave steering," Phys. Rev. Applied, **21**, 044006 (2024). https://doi.org/10.1103/PhysRevApplied.21.044006

[12] X. Zhang, C. Bian, Z. Gong, R. Chen, T. Low, H. Chen, and X. Lin, "Hybrid surface waves in twisted anisotropic heterometasurfaces," Phys. Rev. Applied, **21**, 064034 (2024). https://doi.org/10.1103/PhysRevApplied.21.064034

[13] E. M. Renzi, E. Galiffi, X. Ni, and A. Alù, "Hyperbolic Shear Metasurfaces," Phys. Rev. Lett. **132**, 263803 (2024). https://doi.org/10.1103/PhysRevLett.132.263803

[14] C. Bian, X. Zhang, W. Ma, X. Chen, H. Chen, T. Low, and X. Lin, "Antihyperbolic surface waves on hyperbolic metasurfaces," Phys. Rev. A, **111**, 033522 (2025). https://doi.org/10.1103/PhysRevA.111.033522

[15] X. Zhang, X. Cui, T. Cai, W. Cai, T. Low, H. Chen, and X. Lin, "Scattering-free Plasmonic Brewster Effect via Metasurfaces," ACS Photonics, **12**(4), 1865–1872 (2025). https://doi.org/10.1021/acsphotonics.4c02263

[16] R. Ogier, Y. Fang, M. Käll, and M. Svedendahl, "Near-Complete Photon Spin Selectivity in a Metasurface of Anisotropic Plasmonic Antennas," Phys. Rev. X, **5**, 041019 (2015). https://doi.org/10.1103/PhysRevX.5.041019

[17] S. Droulias and L. Bougas, "Chiral sensing with achiral anisotropic metasurfaces," Phys. Rev. B, **104**, 075412 (2021). https://doi.org/10.1103/PhysRevB.104.075412

[18] C. L. Cortes, W. Newman, S. Molesky, and Z. Jacob, "Quantum nanophotonics using hyperbolic metamaterials," J. Opt. **14**, 063001 (2012). https://doi.org/10.1088/2040-8978/14/6/063001

[19] N. K. Paul, D. Correas-Serrano, and J. S. Gomez-Diaz, "Giant lateral optical forces on Rayleigh particles near hyperbolic and extremely anisotropic metasurfaces," Phys. Rev. B, **99**, 121408(R) (2019). https://doi.org/10.1103/PhysRevB.99.121408

[20] Y. Zhang, M. Antezza, H.-L. Yi, and H.-P. Tan, "Metasurface-mediated anisotropic radiative heat transfer between nanoparticles," Phys. Rev. B, **100**, 085426 (2019). https://doi.org/10.1103/PhysRevB.100.085426

[21] B.-Q. Lin, J.-X. Guo, P. Chu, W.-J. Huo, Z. Xing, B.-G. Huang, and L. Wu, "Multiple-Band Linear-Polarization Conversion and Circular Polarization in Reflection Mode Using a Symmetric Anisotropic Metasurface," Phys. Rev. Applied, **9**, 024038 (2018). https://doi.org/10.1103/PhysRevApplied.9.024038

[22] C.P. Mavidis, A.C. Tasolamprou, E.N. Economou, C.M. Soukoulis, and M. Kafesaki, "Polaritonic cylinders as multifunctional metamaterials: Single scattering and effective medium description," Phys. Rev. B, **102**, 155310 (2020). https://doi.org/10.1103/PhysRevB.102.155310

[23] Y. Nakata, Y. Urade, K. Okimura, T. Nakanishi, F. Miyamaru, M.W. Takeda, and M. Kitano, "Anisotropic Babinet-Invertible Metasurfaces to Realize Transmission-Reflection Switching for Orthogonal Polarizations of Light," Phys. Rev. Applied, **6**, 044022 (2016). https://doi.org/10.1103/PhysRevApplied.6.044022

[24] Y. Nakata, K. Fukawa, T. Nakanishi, Y. Urade, K. Okimura, and F. Miyamaru, "Reconfigurable Terahertz Quarter-Wave Plate for Helicity Switching Based on Babinet Inversion of an Anisotropic Checkerboard Metasurface," Phys. Rev. Applied, **11**, 044008 (2019). https://doi.org/10.1103/PhysRevApplied.11.044008

[25] J. D. Jackson, *Classical Electrodynamics*, 3rd ed. (John Wiley & Sons, New York, 1999).

ВИНИКНЕННЯ ВІД'ЄМНОЇ ДИСПЕРСІЇ ЕЛЕКТРОМАГНІТНИХ ХВИЛЬ У ТВЕРДОТІЛЬНІЙ СТРУКТУРІ, ЩО МІСТИТЬ ПЛАЗМОПОДІБНЕ СЕРЕДОВИЩЕ ТА ПЛАЗМОННІ МЕТАПОВЕРХНІ

Ю.О. Аверков, О.Ю. Аверков, М.М. Білецький

Інститут радіофізики та електроніки ім. О. Я. Усикова НАН України, вул. Акад. Проскури, 12, Харків, 61085, Україна

У цьому дослідженні представлено детальний теоретичний і чисельний аналіз дисперсійних властивостей *p*-поляризованих електромагнітних хвиль у складній багатошаровій твердотільній структурі. Досліджувана система являє собою шестишарову структуру, що містить дві ізотропні плазмонні метаповерхні, які розділені діелектричними прошарками та розташовані на напівнескінченній плазмоподібній підкладці — або сильно легованому напівпровіднику, або металі. Поєднуючи формалізм матриць переносу з рівняннями Максвелла та строгими граничними умовами, ми вивели точні дисперсійні рівняння як для поверхневих, так і для об'ємно-поверхневих мод. Наші чисельні результати вказують на процес каскадної гібридизації між фундаментальними резонансами метаповерхонь і власними поверхневими плазмон-поляритонними (ППП) модами підкладки. Особливо значущим результатом є те, що регулювання ефективних сил осциляторів метаповерхонь викликає виражену дисперсійну асиметрію. Це відбувається тоді, коли одна метаповерхня виявляє ємнісний відгук, тоді як інша стає ефективно індуктивною. Такий електродинамічний дисбаланс призводить до аномального режиму негативної частотної дисперсії, що характеризується поширенням зворотних хвиль. Крім того, ми демонструємо, що модифікація діелектричного оточення або заміна напівпровідникової підкладки на металеву зміщує області резонансної взаємодії, пропонуючи універсальний засіб керування спектральними інтервалами розщеплення мод. Ці висновки створюють міцне теоретичне підґрунтя для проєктування перебудовуваних нанофотонних пристроїв та генерації розподіленого внутрішнього зворотного зв'язку, що є необхідним для виникнення абсолютних нестійкостей електромагнітних хвиль у системах, пов'язаних із пучками заряджених частинок.

Ключові слова: *плазмонна метаповерхня; гібридна поверхнева хвиля; об'ємно-поверхнева хвиля; від'ємна дисперсія; напівпровідникова підкладка; гібридизація мод*